Wireless, flexible, ionic, perspiration-rate sensor system with long-time and high sweat volume functions toward early-stage, real-time detection of dehydration

*Satoko Honda[1†], Ryuki Tanaka[1†], Guren Matsumura[1], Naruhito Seimiya[1], Kuniharu Takei[1,2]**

[1]Department of Physics and Electronics, Osaka Metropolitan University, Naka-ku, Sakai, Osaka 599-8531, Japan

[2]Graduate School of Information Science and Technology, Hokkaido University, Kita-ku, Sapporo, Hokkaido 060-0814, Japan

†These authors contributed equally.

*Corresponding author: takei@ist.hokudai.ac.jp

Keywords: flexible sensor, perspiration rate, ion concentration, wearable sensor, wireless system

Abstract

Flexible sensors that can be attached to the body to collect vital data wirelessly enable real-time, early-stage diagnosis for human health management. Wearable sweat sensors have received considerable attention for real-time physiological monitoring. Unlike conventional methods that require blood-drawing in a clinic, sweat analyses may enable non-invasive tracking of health conditions for early-stage diagnosis. Even though a variety of studies to monitor metabolites and other substances have been conducted, automatic, continuous, long-term, simultaneous monitoring of perspiration rate and electrolytes, which are important parameters in dehydration, has yet to be achieved because of challenges related to sensor design. Here we present a wireless, wearable, integrated, microfluidic sensor system that can continuously measure these parameters in real-time for prolonged periods. The proposed sensors are systematically characterized, and machine learning is used to predict device tilt angle to calibrate sensor output signals. Using the

sensor design to form a water droplet in a fluidic channel, high-volume perspiration rate is continuously monitored for more than 7000 s (total sweat volume >170 μL). By testing 10 subjects, physiological responses to ingestion of a sports drink were confirmed by measuring perspiration rhythm changes extracted from real-time, continuous sweat impedance and rate.

Introduction

Innovations in sensing technology contribute to comfortable, convenient, healthy life-styles, and smart self-healthcare encourages people to take a proactive approach to early-stage disease prevention. This trend, in which individuals monitor their health status in real-time, may eventually lead to self-diagnosis of diseases. For realization of such a goal, a multimodal, wearable sensor system is essential technology[1-3]. A wearable sensor attached to the skin enables detection of biological information[1] such as skin temperature [4,5], cardiac performance (electrocardiogram) [6-8], respiration [9,10], perspiration [11-13], and chemicals [14-19] from sweat in real-time. Unlike conventional personal-use medical equipment, continuous real-time biological information can track rhythms of biological parameters. Chemical substances in sweat contain considerable information regarding electrolytes, metabolites, pH, uric acid, and amino acids, etc., offering valuable insights as biomarkers [20-25]. Sweat is an attractive biological fluid because unlike blood, it can be acquired non-invasively, for continuous, real-time monitoring.

Perspiration may be induced by heat, trans-epidermal water loss[26], or psychological stress [27]. Thermal perspiration involves a time lag before sweat glands begin to secrete, whereas mental perspiration occurs rapidly. Trans-epidermal water loss is invisible, unlike thermal and mental perspiration, and it occurs from the surface of the skin rather than from sweat glands. Thermal perspiration caused by high environmental temperature or physical exercise helps restore body core temperature through evaporative cooling. However, excessive sweating causes a loss of water and electrolytes, which can lead to dehydration, and cardiac and nervous system abnormalities. While the importance of replenishing water and electrolytes lost through sweating

is widely understood, it is still difficult to continuously monitor sweat composition for long periods during rapid sweating.

To monitor perspiration rate and electrolytes in sweat, fluidic channel structures on a flexible film have been reported [20,28]. These devices can continuously analyze the amount of perspiration, total ion quantities, and ion concentration in sweat, but once the fluidic channel is filled, no further measurements are possible [13,29,30]. Another reported approach is to measure droplet flowmetry in real-time[31]. In principle, this method allows long-term perspiration rate measurement without having to fill the channel with sweat. However, since the device is exposed to the atmosphere, evaporation is unavoidable, leading to inaccurate measurements. Also, a large area is required for the sweat collection network needed for droplet formation. Another approach is to evacuate sweat in the channel[12], but this requires manual operation. Another approach uses capillary action of cotton fibers to remove old perspiration and supply fresh perspiration in the sensor[32]. However, since cotton fibers are covered with polyurethane, no further measurements are possible once the cotton fibers are filled with sweat. Importantly, most reports have focused on either the perspiration rate or electrolytes in sweat. Due to the difficulty of addressing all challenges simultaneously, autonomous, highly accurate, and long-term continuous measurements of perspiration rate and electrolyte contents simultaneously have not yet been achieved.

To address this challenge, in this study, we devised a wireless, wearable, integrated sensor system (Figure 1a). The sweat rate and ion sensors are integrated on a polyethylene terephthalate (PET) film (Figure 1b). The fluidic channels comprise three parts: a top fluidic channel that collects and releases sweat, a chamber junction that forms and discharges droplets of sweat, and a bottom channel that contains filter paper to quickly discharge the sweat. In the top fluidic channel, a pair of carbon electrodes for impedance sensing and a carbon electrode for perspiration rate sensing are integrated. Another carbon electrode for the perspiration rate sensing is formed in the bottom channel. Released droplets are absorbed by the filter paper and quickly discharged to the outside by capillary action and evaporation. Important features of this configuration are the

chamber junction and shape, which convert continuous flow into constant-volume droplets, and promote rapid absorption of the droplets. Sweat volume is determined by counting and measuring droplet resistance between carbon black (CB) electrodes in the top and bottom channels. Due to electrical conductivity of sweat, electrical resistance can be measured as a droplet moves from the chamber to the filter paper. Perspiration rate can be calculated by measuring time intervals between water droplets, since water droplet volume is almost constant, defined by fluidic channel and chamber designs.

In addition to the sensors, a system with a Bluetooth module for data transmission from sensors to a smartphone app is also developed (Figure 1c-d). After sensor characterization, physiological tests are performed to validate operation of sensor systems and to observe physiological electrolyte changes.

RESULTS AND DISCUSSION

Ion sensor.

First, only the ion sensor was characterized without integrating the perspiration rate sensor. To keep the sensor system simple, total ion concentration in sweat is measured instead of specific electrolytes, such as K^+ and Na^+. Although this is not an accurate evaluation of body electrolytes, trends of individual electrolytes should be similar. For practical healthcare applications, device cost is another factor, and this simplified system addresses this issue. Figures 2a and 2b show cross-sectional schematic and top views of the ion sensor, respectively. The ion sensor consists of silver (Ag) ink for interconnections between the sensor and wireless system, CB electrodes for impedance measurement of sweat, and a PDMS fluidic channel on PET film. Although PET film is not stretchable, it has enough flexibility to attach the sensor system to the arm, forehead, or chest to monitor sweat. All Ag and CB electrodes were printed on the PET film with a screen printer and dispenser, respectively. The distance between the two CB electrodes is 1.3 mm. Once sweat on the skin passes between the CB electrodes, electrical impedance of sweat is measured

at 10 kHz. After measurement of impedance, sweat is discharged from the outlet. To enhance sweat discharge, a piece of a Kimwipe was placed at the outlet, causing sweat to be discharged quickly by capillary action.

To assess fundamental characteristics, NaCl solution was used to imitate sweat. Real-time impedance was measured by repeatedly changing the Na^+ concentration between 0 and 90 mM (Figure 2c). When the NaCl concentration was changed, the sensor showed highly reproducible output. Summarizing impedance values for each concentration in three cycles, slight, nonsignificant hysteresis was observed at low concentrations (Figure 2d). Impedance changes exponentially with concentration, and an approximate curve was obtained to convert impedance values to ion concentrations (Figure S1). Average intervals were extracted from 144 data points with small error bars having high correlation coefficients ~0.996. This demonstrates that sensor output is consistent and reliable.

Sweat impedance monitoring was also conducted to confirm that the sensor can detect sweat impedance continuously and wirelessly. Furthermore, for this test, effects of sports drink (Pocari Sweat, Otsuka Pharmaceutical Co. Ltd.) intake during heavy sweating were analyzed. Ion sensor devices were attached to the foreheads of 10 volunteers during a trial. Volunteers fasted for at least 4 h before this measurement, in order to avoid differences in baseline ionic concentration due to meals. Right before the trial, they drank 200 mL of water to facilitate sweating. Volunteers wore a sauna suit and spent time in a sauna tent to induce sweating rapidly. These volunteers participated in two trials, with/without drinking sports drink. When impedance was stabilized after sweating started, sports drink was consumed. Figure 2e shows representative results with/without sports drink. The beginning of sweat detection was set as 0 min and impedance was normalized to clearly show impedance changes with/without sports drink consumption. The impedance decreased about 14 min after drinking the sports drink, indicating that the ion concentration increased in sweat. On the other hand, the impedance of sweat when drinking only water did not change, which means that ion concentration in sweat is almost constant. Another

trend of ion change is shown in Figure S2a. In the case of sports drink intake, after ~10 min, impedance decreased, and continued to decrease gradually thereafter. On the other hand, without sports drink intake, impedance slowly increases although some impedance drop was observed. Increasing ion concentration was observed in 8 subjects (Figure 2f). Interestingly, the time interval at which ion concentration changed after sports drink intake varied from ~4 to ~15 min, depending on the subject (Figure S2b). This suggests that continuous monitoring is required to detect individual dehydration timing precisely.

Electrode stability for impedance measurements is often problematic, due to fatty acids or other organic components in sweat. To confirm the stability of carbon electrodes used in this study, impedance was monitored 5 times in a week by attaching the same sensor to an arm (Figure S3). Since real sweat impedance was measured, there are small impedance differences day-by-day. Importantly, impedance values and trends are similar for every result, suggesting that fatty acids and/or other organic components have negligible impact on impedance measurements.

Perspiration Rate Sensor

Perspiration rate affects the ion concentration in sweat. Furthermore, it is important to analyze perspiration rate relative to dehydration. To monitor long-term, high perspiration rate continuously, this sensor was developed. The sensing mechanism measures electrical resistance caused by a sweat droplet between two CB electrodes (Figure 3a). Due to the sensor design, a sweat droplet is formed in a chamber, making a brief connection between the electrodes (Figure 3a). After this connection, the droplet is ejected to the bottom channel by a filter paper (Figure 3b). While there was no droplet in the chamber before sweat flow commenced (Figure 3c), droplets were formed, connecting the top and bottom electrodes (Figure 3d). To form a water droplet in the chamber, the microfluidic channels should be hydrophobic. Due to surface tension of water and hydrophobicity of channel, when water exits the top channel to the chamber, a droplet is formed until it reaches the filter paper. It is worth noting that water droplets do not form if the channel and chamber surfaces are hydrophilic due to adhesion and spreading of the water in the

chamber. At a flow of 0.6 μL/min from the inlet, a resistance peak appears roughly every 40 s (Figure 3e). Importantly, once the growing droplet reaches the bottom channel, the measurement circuit detects the low-resistance immediately, followed by a return to high-resistance after < 3 s (Figure 3e inset).

This study integrated the perspiration rate sensor with the ion sensor located before the chamber of the perspiration rate sensor. For this purpose, a longer top channel is required to incorporate the impedance sensor. To optimize the length of the top channel, intervals between peaks were compared for devices with different top channel lengths. When comparing devices with top channel lengths of 3 mm and 6 mm, the longer channel length had slightly lower reproducibility, but it was not significantly different (3 mm: 39.57±1.41 s, 6 mm: 41.75±5.36) (Figure 3f), indicating that top channel length does not affect output signals. Channel width and height were fixed at 0.8 mm and 0.22 mm, respectively.

Next, chamber shape was studied to generate continuous flow of constant-volume droplets, which is essential for this sweat sensor. Four chamber shapes (heart-shaped, round, square, and triangular) were prepared to determine which is most suitable for formation of the droplet stream (Figure 3g). Regardless of shape, the interval was around 40 s in all cases; however, variation was larger for round and triangular shaped chambers (Figure 3h). Droplets spread over the top part of the chamber in the round, square, and triangular shapes most likely due to capillary action at the edge of chamber (Figure 3g). The square chamber showed obvious water spreading. This water spreading at the edge of chamber caused unstable droplet formation and longer intervals. Based on these results, the heart-shaped chamber had the most stable intervals, most likely caused by forming droplets of constant volume without spreading on the side wall of the chamber and by quickly draining them into the filter paper. Due to this stable operation, the heart-shaped chamber was used for further study of the perspiration rate sensor.

Due to water droplet absorption from the chamber, filter paper tip shape may affect accuracy and speed. To investigate this effect, three tip shapes were tested (Figure 3i). First, using two

shapes (F2 and T2), width, *W*, was changed from 0.3 mm to 1.0 mm (Figure S4). Although different widths and different shapes had almost the same characteristics (Figure 3i and S4), *W*=0.8 mm of F2 offered the best reproducibility. This is mostly because the contact surface is large and flat, increasing the probability to contact the droplet to the filter at the same volume, whose shape is slightly changed by various conditions such as tilting angle. After optimizing the structure of the fluidic channel, intervals were exponentially changed as a function of flow rate, and an approximate curve was obtained (Figure S5). The correlation coefficient of the curve fitting was 0.986, and all trends extracted from 500 data points were similar. Thus, the perspiration rate sensor is reliable and reproducible. From the equation for the curve, intervals were converted to flow rates.

The sensor is installed vertically and droplets are formed under the top channel due to droplet mass. For wearable applications, the sensor is often tilted, depending on activity. Therefore, it is necessary to check tilt angle dependence and to calibrate the angle dependence for accurate perspiration rate monitoring. Tilt angle was defined as 0° for a vertical state. The sensor was moved from 0° to a horizontal state, i.e. 90°, in 10° increments, and when it reached 90°, it was returned to its original position. Intervals up to 70° are almost constant at around 40 s whereas the interval increased significantly over 80° (Figure 3j). However, it returned to the original interval when the sensor returned to 0°. This suggests that below 70°, the attractive force of droplet surface energy and the hydrophobic surface of the channel are stronger than the force of gravity but that gravitational force is stronger above ~80°. The tilt angle is required to measure perspiration rate accurately for wearable device applications. Detection of this angle is discussed later using a simple machine learning method.

The most important attribute of this sensor is the capacity to measure the perspiration rate for a long time at high flow. Optimized microfluidic structure was determined by supplying water with a syringe pump at ~1.4 μL/min. Since a large volume of water cannot be absorbed by the filter paper, a water-absorbent polymer sheet used for baby diapers was placed on the surface of

the filter paper. As a result, the sensor can monitor perspiration rate continuously up to ~7300 s with ~8 % fluctuation (Figure 3k). However, after 7300 s, the interval increases slightly, and after 12000 s the intervals suddenly increase drastically with large fluctuations. This large change is because water droplets in the chamber cannot be absorbed into the filter paper quickly enough, such that the top and bottom channels are connected longer, which causes longer intervals and poor reliability. Although this device is still somewhat limited in terms of sweat volume, this device accepts a continuous measurable sweat volume >11 times larger than sensors for electrical sensing[12,29] and ~1.3 times larger than sensors for color change monitoring[13] reported previously.

After sensor properties were confirmed with long-term measurements, sensor output reliability was investigated by comparing a commercially available sweat sensor (SKW-1000, Skinos Ltd.). Both sensors were attached to a subject's forearms to observe the measured sweat rates simultaneously (Figure 3l). Because the commercial sensor detects humidity in the chamber where it is attached, it detects perspiration immediately, and the perspiration gradually increases after 700 s. After ~1300 s, our sensor also begins to detect perspiration and shows similar behavior in terms of perspiration rate until about 2400 s. Similar trends were recorded by both sensors between 1300 and 2300 s. Unfortunately, the commercial sensor cannot discharge perspiration, so the amount of sweat it could measure was limited. For this reason, the commercial sensor was stopped and removed at ~2400 s, and it could not be used to compare results of this flexible perspiration sensor.

In order to calibrate the tilt angle dependence of the sweat rate sensor, data from the accelerometer/gyro sensor installed in the wireless circuit system attached to the arm with the sensor was used to detect the tilt angle, using a logistic regression function (Figure 4a). After optimizing algorithms of machine learning, we decided that only x-axis output should be used to predict angles. X-axis output was measured for three cycles while changing the angle of the

accelerometer from 0° to 90° and vice versa in 10° increments (Figure 4b). Data were divided into training data (two cycles of changing the angle from 0° to 90° and 90° to 0°) and test data (one cycle of changing the angle from 0° to 90° and 90° to 0°). Then, the detection model was evaluated by introducing cross-validation to assess its generalization performance. The average accuracy was 0.997, which indicated almost perfect angle prediction (Figure 4c-d).

Integrated sweat sensor

As a proof-of-concept for the wireless, ionic, perspiration rate monitoring system, two sensors were integrated on a PET film (Figure 5a), and these were assembled with a wireless/acceleration sensor system (Figure 5b). The system consisted of a microcomputer, an impedance measurement module, a resistance sensing module, an analog/digital converter, a low-energy Bluetooth (BLE) module, and a battery. Medical adhesive tape (Perme-role) was attached to the back of the sensor sheet for bonding to the skin. A 3-mm hole was formed for sweat to enter the fluidic channel (Figure S6). Subjects sweated in a sauna tent. They participated in two trials, one with only water intake and the other with sports drink during measurements, in addition to water taken before measurement. Output signals from the X-axis of the acceleration sensor (Figure 5c) predicted the sensor angle (Figure 5d) extracted from a machine-learning algorithm using the results of Figure 5c. Perspiration rate (Figure 5e) and normalized sweat impedance (Figure 5f) are shown. Based on these results, this wireless integrated sensor sheet can measure perspiration rate and sweat impedance corresponding to the ion level simultaneously for long periods with a high perspiration rate. Since these are physiological parameters, subjects differ in how sports drinks are metabolized and excreted as sweat. For more detailed discussion, physiological tests with much larger numbers of subjects are required to evaluate electrolyte changes caused by sports drink, which beyond the scope of this study.

Conclusion

This study developed a wireless integrated ion and perspiration rate sensor sheet for

dehydration monitoring. By developing a new sensor structure, ion composition and perspiration rate can be monitored simultaneously for a long period. Both sensors show good repeatability and reproducibility with low hysteresis. Although the perspiration rate sensor has tilt-angle dependence, this can be calibrated by predicting the tilt angle using a logistic regression algorithm. Using a droplet formation method in a fluidic channel, high-volume perspiration was continuously detected for more than 7000 s. Importantly, by developing an integrated sensor system and by optimizing the device structure, continuous monitoring of a large total sweat volume corresponding to long-term measurement was realized. This sensor can measure a total sweat volume of 170 μL continuously, which is >11 and ~1.3 times larger volume than volumes reported for electrical monitoring[12, 29] and color change sensors[13], respectively. Finally, as proof-of-concept, real-time wireless simultaneous monitoring of sweat ion concentration and volume were conducted using the wireless system with data transfer to a smartphone app in real-time. Furthermore, the effect of sports drink ingestion was observed from sensor output. Although physiological results of this study are still preliminary, this sensor system may allow early prediction of dehydration from sweat ionic composition and perspiration rate. While there is still much more work to do before practical applications for monitoring human health, this system is a good platform to demonstrate benefits of flexible healthcare electronics.

Experimental Methods

Device Fabrication: The sweat sensor consists of ion concentration and sweat rate sensors on a flexible film (Figure 1a). First, silver (Ag) electrodes were screen-printed on a PET film (38 μm thick). Subsequently, CB electrodes were printed on the patterned Ag electrodes using a dispensing machine. After cutting the PET film, a 1.8-mm^2 inlet hole for sweat from skin to the microfluidic channel was punched on the PET substrate. Then, the patterned device on a PET substrate was treated with O_2 plasma and APTES, prior to strong bonding to the PDMS fluidic channel. The PDMS fluidic channel was made using the mold method. The mold pattern was

prepared by cutting PET films (125 μm thick) laminated onto a plastic petri dish. PDMS was mixed at a 10:1 weight% ratio of base : curing agent and degassed under vacuum for 1 h. Degassed PDMS was poured onto the mold and cured for 1 h at 90 °C. Subsequently, the cured PDMS was peeled from the mold. PDMS was treated with O_2 plasma and bonded to the APTES-treated PET substrate. A cut filter paper (0.22 mm thick) (No. 5A, Advantec MFS) was sandwiched between the PET film and PDMS. In addition, the filter paper was fixed on the PET film by covering the PET film with double-sided tape. Ag electrodes were covered with PDMS for insulation. Even after bending the device, no delamination or cracking occurred in the sensors during handling.

Sensor Characterization: Signals of the ion and perspiration rate sensors were acquired using a home-made wireless circuit system. Off-body measurements using the ion sensor were obtained using NaCl solutions with different concentrations. For off-body measurement with the perspiration rate sensor, tap water or colored tap water were used. Controlled flow rate experiments were carried out using a syringe pump (YSP-301, YMC Co., Ltd.).

Physiological experiments

Foreheads or forearms of participants were wiped and cleaned with alcohol gauze before attaching the sensing sheet with adhesive tape. Subjects wore sauna suits and stayed in the sauna tent to sweat. Data were transferred from the circuit to the smartphone via Bluetooth, and results were displayed in real-time on the smartphone monitor (Figure 1d). Human subject experiments were performed in compliance with a protocol approved by the ethics committee at Osaka Metropolitan University. Informed consent was obtained from all volunteers to record and use all data.

Supporting Information

Supporting Information is available from the Wiley Online Library or from the author.

Acknowledgements

This work was partially supported by JST AIP Accelerated Program (No. JPMJCR21U1), JSPS KAKENHI (Grant No. JP22H00594), the Murata Science Foundation, the Hitachi Global Foundation, and the Takeda Science Foundation.

Conflict of Interest

The authors declare no conflict of interest.

Data Availability Statement

The data that support the findings of this study are available from the corresponding author upon reasonable request.

Received: ((will be filled in by the editorial staff))
Revised: ((will be filled in by the editorial staff))
Published online: ((will be filled in by the editorial staff))

References

[1] Y. Luo, M. R. Abidian, J. H. Ahn, D. Akinwande, A. M. Andrews, M. Antonietti, Z. Bao, M. Berggren, C. A. Berkey, C. J. Bettinger, J. Chen, P. Chen, W. Cheng, X. Cheng, S. J. Choi, A. Chortos, C. Dagdeviren, R. H. Dauskardt, C. A. Di, M. D. Dickey, X. Duan, A. Facchetti, Z. Fan, Y. Fang, J. Feng, X. Feng, H. Gao, W. Gao, X. Gong, C. F. Guo, X. Guo, M. C. Hartel, Z. He, J. S. Ho, Y. Hu, Q. Huang, Y. Huang, F. Huo, M. M. Hussain, A. Javey, U. Jeong, C. Jiang, X. Jiang, J. Kang, D. Karnaushenko, A. Khademhosseini, D. H. Kim, I. D. Kim, D. Kireev, L. Kong, C. Lee, N. E. Lee, P. S. Lee, T. W. Lee, F. Li, J. Li, C. Liang, C. T. Lim, Y. Lin, D. J. Lipomi, J. Liu, K. Liu, N. Liu, R. Liu, Y. Liu, Y. Liu, Z. Liu, Z. Liu, X. J. Loh, N. Lu, Z. Lv, S. Magdassi, G. G. Malliaras, N. Matsuhisa, A. Nathan, S. Niu, J. Pan, C. Pang, Q. Pei, H. Peng, D. Qi, H. Ren, J. A. Rogers, A. Rowe, O. G. Schmidt, T. Sekitani, D. G. Seo, G. Shen, X. Sheng, Q. Shi, T. Someya, Y. Song, E. Stavrinidou, M. Su, X. Sun, K. Takei, X. M. Tao, B. C. K. Tee, A. V. Thean, T. Q. Trung, C. Wan, H. Wang, J. Wang, M. Wang, S. Wang, T. Wang, Z. L. Wang, P. S. Weiss, H. Wen, S. Xu, T. Xu, H. Yan, X. Yan, H. Yang, L. Yang, S. Yang, L. Yin, C. Yu, G. Yu, J. Yu, S. H. Yu, X. Yu, E. Zamburg, H. Zhang, X. Zhang, X. Zhang, X. Zhang, Y. Zhang, Y. Zhang, S. Zhao, X. Zhao, Y. Zheng, Y. Q. Zheng, Z. Zheng, T. Zhou, B. Zhu, M. Zhu, R. Zhu, Y. Zhu, Y. Zhu, G. Zou, X. Chen, *ACS Nano* **2023**, 17, 5211.

[2] K. Xu, Y. Lu, K. Takei, *Adv. Funct. Mater.* **2021**, 31, 2007436.

[3] K. Xu, Y. Lu, K. Takei, *Adv. Mater. Technol.* **2019**, 4, 1800628.

[4] K. Xu, Y. Lu, T. Yamaguchi, T. Arie, S. Akita, K. Takei, *ACS Nano* **2019**, 13, 14348.

[5] Y. Yamamoto, S. Harada, D. Yamamoto, W. Honda, T. Arie, S. Akita, K. Takei, *Sci. Adv.*

2016, 2, e1601473.

[6] M. Takaya, R. Matsuda, G. Inamori, U. Kamoto, Y. Isoda, D. Tachibana, F. Nakamura, O. Fuchiwaki, Y. Okubo, H. Ota, *ACS Sens.* **2021**, 6, 212.

[7] Y. Xuan, H. Hara, S. Honda, Y. Li, Y. Fujita, T. Arie, S. Akita, K. Takei, *Appl. Phys. Rev.* **2022**, 9, 011425.

[8] S. Imani, A. J. Bandodkar, A. M. Mohan, R. Kumar, S. Yu, J. Wang, P. P. Mercier, *Nat. Commun.* **2016**, 7, 11650.

[9] Z. Zhou, S. Padgett, Z. Cai, G. Conta, Y. Wu, Q. He, S. Zhang, C. Sun, J. Liu, E. Fan, K. Meng, Z. Lin, C. Uy, J. Yang, J. Chen, *Biosens. Bioele.* **2020**, 155, 112064.

[10] K. Xu, Y. Fujita, Y. Lu, S. Honda, M. Shiomi, T. Arie, S. Akita, K. Takei, *Adv. Mater.* **2021**, 33, e2008701.

[11] S. Liu, D. S. Yang, S. Wang, H. Luan, Y. Sekine, J. B. Model, A. J. Aranyosi, R. Ghaffari, J. A. Rogers, *EcoMat* **2022**, 5, e12270.

[12] M. Bariya, N. Davis, L. Gillan, E. Jansson, A. Kokkonen, C. McCaffrey, J. Hiltunen, A. Javey, *ACS Sens.* **2022**, 7, 1156.

[13] L. B. Baker, J. B. Model, K. A. Barnes, M. L. Anderson, S. P. Lee, K. A. Lee, S. D. Brown, A. J. Reimel, T. J. Roberts, R. P. Nuccio, J. L. Bonsignore, C. T. Ungaro, J. M. Carter, W. Li, M. S. Seib, J. T. Reeder, A. J. Aranyosi, J. A. Rogers, R. Ghaffari, *Sci. Adv.* **2020**, 6, eabe3929.

[14] W. Gao, S. Emaminejad, H. Y. Nyein, S. Challa, K. Chen, A. Peck, H. M. Fahad, H. Ota, H. Shiraki, D. Kiriya, D. H. Lien, G. A. Brooks, R. W. Davis, A. Javey, *Nature* **2016**, 529, 509.

[15] T. R. Ray, M. Ivanovic, P. M. Curtis, D. Franklin, K. Guventurk, W. J. Jeang, J. Chafetz, H. Gaertner, G. Young, S. Rebollo, J. B. Model, S. P. Lee, J. Ciraldo, J. T. Reeder, A. Hourlier-Fargette, A. J. Bandodkar, J. Choi, A. J. Aranyosi, R. Ghaffari, S. A. McColley, S. Haymond, J. A. Rogers, *Sci. Tranl. Med.* **2021**, 13, eabd8109.

[16] Y. Yang, Y. Song, X. Bo, J. Min, O. S. Pak, L. Zhu, M. Wang, J. Tu, A. Kogan, H. Zhang, T. K. Hsiai, Z. Li, W. Gao, *Nat. Biotech.* **2019**, 38, 217.

[17] J. R. Sempionatto, M. Lin, L. Yin, E. De la Paz, K. Pei, T. Sonsa-Ard, A. N. de Loyola Silva, A. A. Khorshed, F. Zhang, N. Tostado, S. Xu, J. Wang, *Nat. Biomed. Eng.* **2021**, 5, 737-748.

[18] Y. Yang, W. Gao, *Chem. Soc. Rev.* **2019**, 48, 1465-1491.

[19] S. Nakata, M. Shiomi, Y. Fujita, T. Arie, S. Akita, K. Takei, *Nat. Electron.* **2018**, 1, 596.

[20] C. Wang, E. Shirzaei Sani, W. Gao, *Adv. Funct. Mater.* **2021**, 32, 2111022.

[21] J. Tu, J. Min, Y. Song, C. Xu, J. Li, J. Moore, J. Hanson, E. Hu, T. Parimon, T.-Y. Wang, E. Davoodi, T.-Fu. Chou, P. Chen, J. J. Hsu, H. B. Rossiter, W. Gao, *Nat. Biomed. Eng.* **2023** DOI: 10.1038/s41551-023-01059-5.

[22] J. Min, J. Tu, C. Xu, H. Lukas, S. Shin, Y. Yang, S. A. Solomon, D. Mukasa, W. Gao, *Chem. Rev.* **2023**, 123, 5049-5138.

[23] J. R. Sempionatto, J. A. Lasalde-Ramirez, K. Mahato, J. Wang, W. Gao, *Nat. Rev. Chem.* **2022**, 2022, 6, 899-915.

[24] T. Saha, R. D. Cano, K. Mahato, E. D. I. Paz, C. Chen, S. Ding, L. Yin, J. Wang, *Chem. Rev.* **2023**, DOI: 10.1021/acs.chemrev.3c00078.

[25] N. K. Singh, S. Chung, A. Chang, J. Wang, D. A. Hall, *Biosens. & Bioele.* **2023**, 227, 115097.

[26] J. B. Schwarck, C. A. Burdon, E. A. Taylor, G. E. Peoples, C. A. Machado-Moreira, N. A. S. Taylor, *J. Therm. Biol.* **2019**, 82, 242.

[27] Y. Kuno, *https://www.jstage.jst.go.jp/article/jspfsm1949/14/2/14_2_1/_pdf*.

[28] S. Li, Z. Ma, Z. Cao, L. Pan, Y. Shi, *Small* **2020**, 16, e1903822.

[29] Z. Yuan, L. Hou, M. Bariya, H. Y. Y. Nyein, L. C. Tai, W. Ji, L. Li, A. Javey, *Lab Chip* **2019**, 19, 3179.

[30] H. Y. Y. Nyein, M. Bariya, L. Kivimaki, S. Uusitalo, T. S. Liaw, E. Jansson, C. H. Ahn, J. A. Hangasky, J. Zhao, Y. Lin, T. Happonen, M. Chao, C. Liedert, Y. Zhao, L.-C. Tai, J. Hiltunen, A. Javey, *Sci. Adv.* **2019**, 5, eaaw9906.

[31] Y. Yang, S. Xing, Z. Fang, R. Li, H. Koo, T. Pan, *Lab. Chip* **2017**, 17, 926.

[32] C. W. Bae, P. T. Toi, B. Y. Kim, W. I. Lee, H. B. Lee, A. Hanif, E. H. Lee, N. E. Lee, *ACS Appl. Mater. Interfaces* **2019**, 11, 14567.

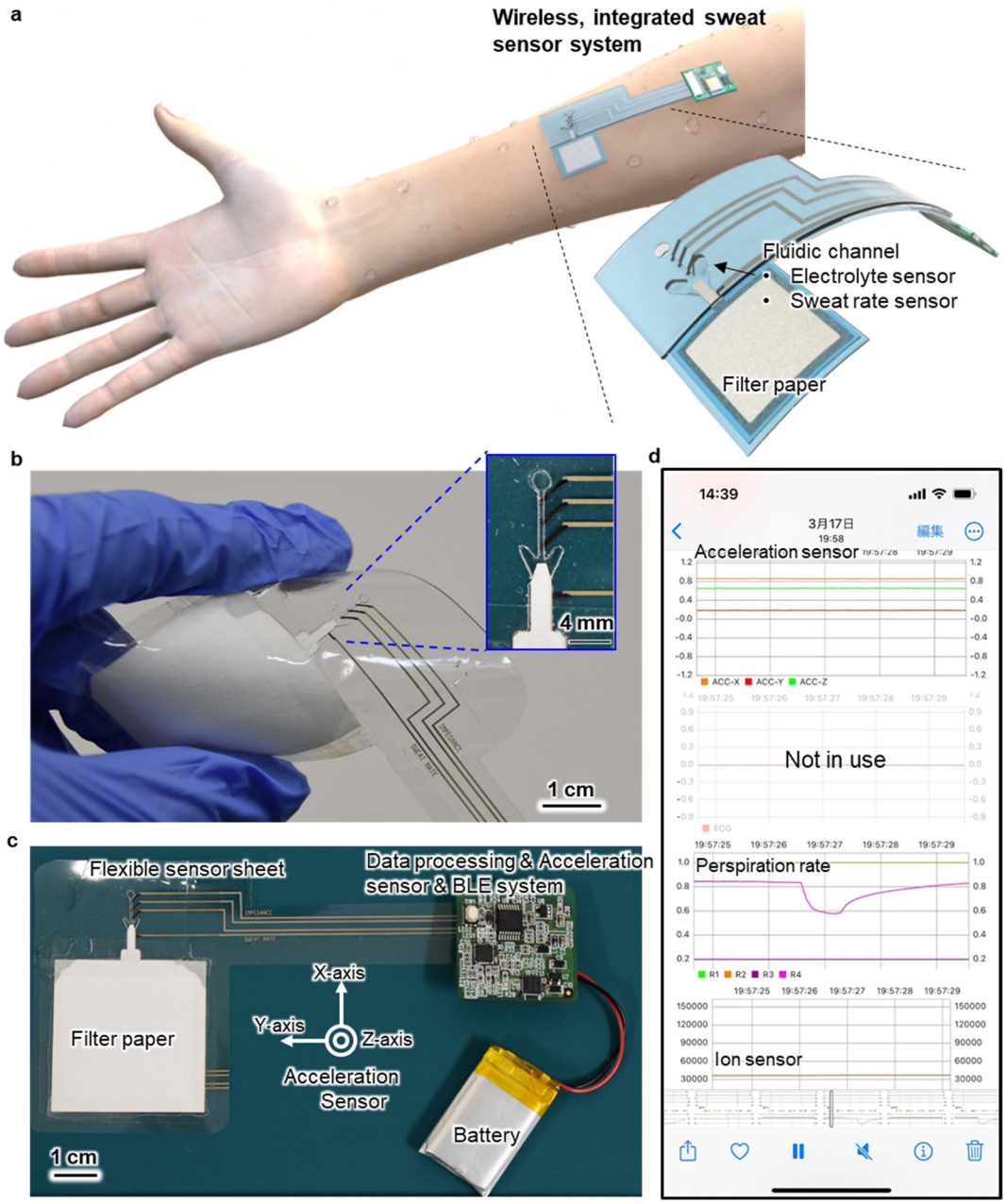

Figure 1. Wireless integrated ion and perspiration rate sensor system. (a) Schematic of the flexible sweat sensor sheet with an integrated ion sensor and sweat rate sensor. Photos of (b) the sweat sensor and an enlarged image of the fluidic channel region and (c) total system of the wireless integrated sensor. (d) Display of the smartphone app during measurement.

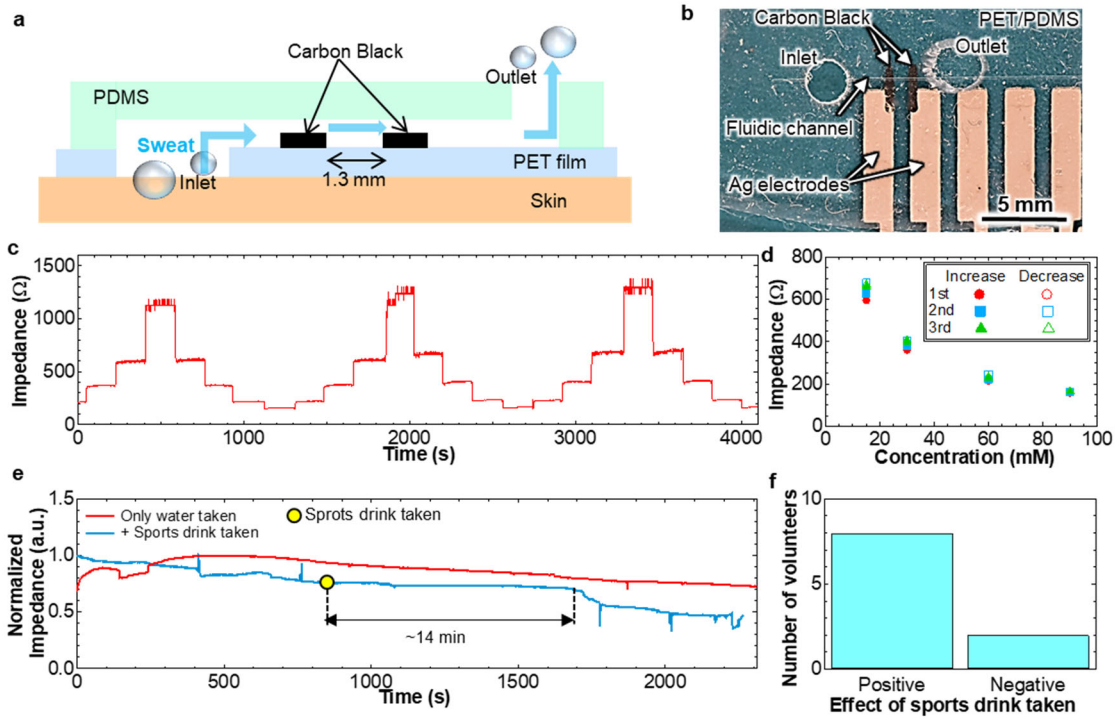

Figure 2. Ion impedance sensor. (a) Cross-sectional schematic of the ion sensor. (b) Top view of the ion sensor. (c) Cycle tests of impedance measurements of the ion sensor between 0 and 90 mM NaCl. (d) Trend of impedance changes during multiple cycles at varied Na^+ concentrations extracted from (c). (e) Real-time sweat impedance monitoring with/without sports drink taken during measurement. (f) Volunteers who had a sweat impedance change (positive) and those who did not (negative) after sports drink intake.

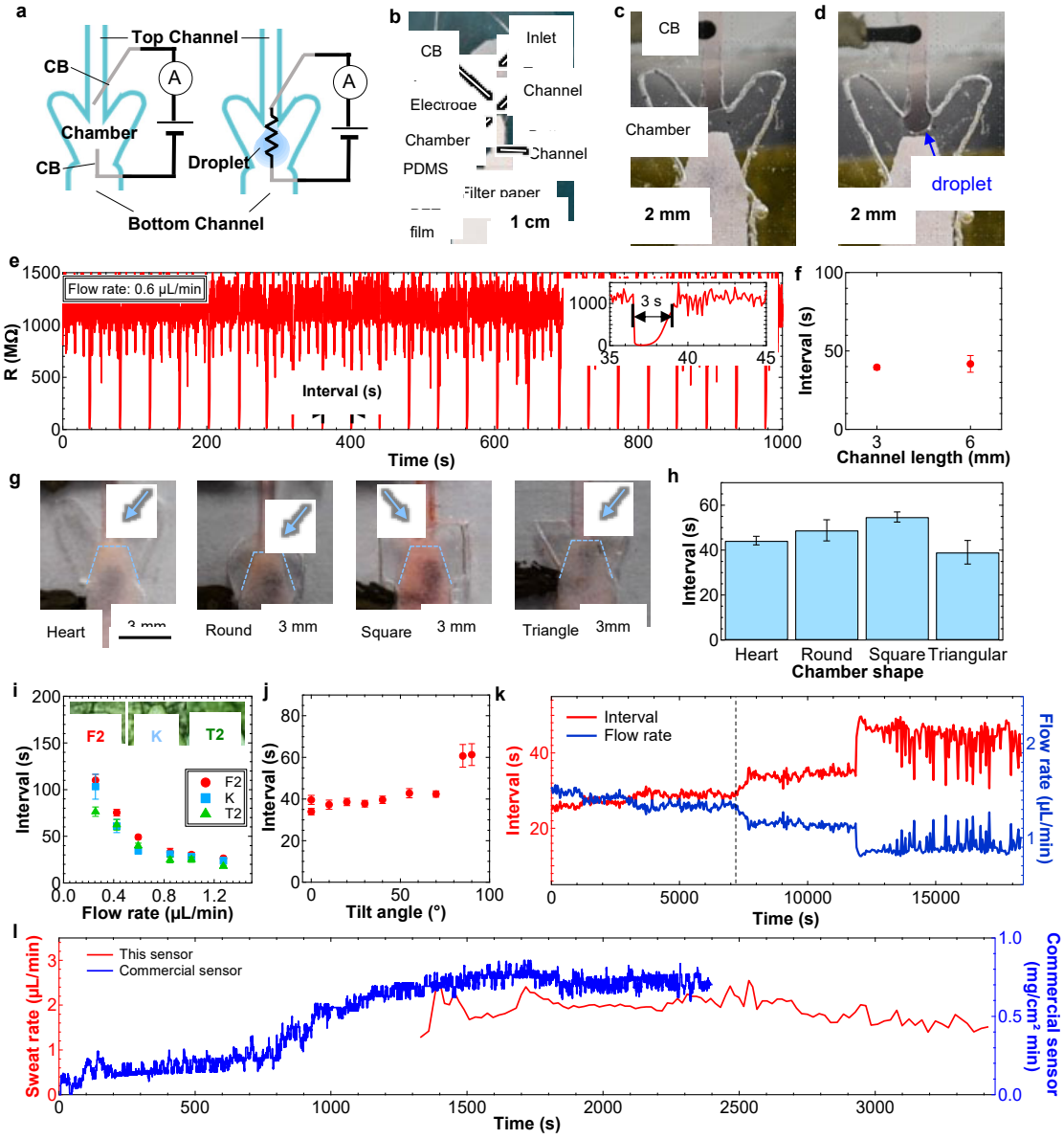

Figure 3. Perspiration rate sensor. (a) Schematic of the sweat rate sensing mechanism. (b) Photo of the sensor. Photos (c) without and (d) with droplets in the chamber. (e) Continuous resistance monitoring at a flow rate of 0.6 μL/min. Inset is the resistance change during one droplet process. (f) Intervals between top channels 3 mm and 6 mm in length. (g) Photos of each chamber shape and droplets formed. (h) Compiled intervals at different shapes of each chamber. (i) Intervals as a function of flow rate using different shapes of filter paper. (j) Interval as a function of tilt angle. (k) Long-term measurement at 1.4 μL/min and flow rate calculated by the equation. (l) Real-time sweat rate measurement using commercial sweat rate sensor and the sensor of this study.

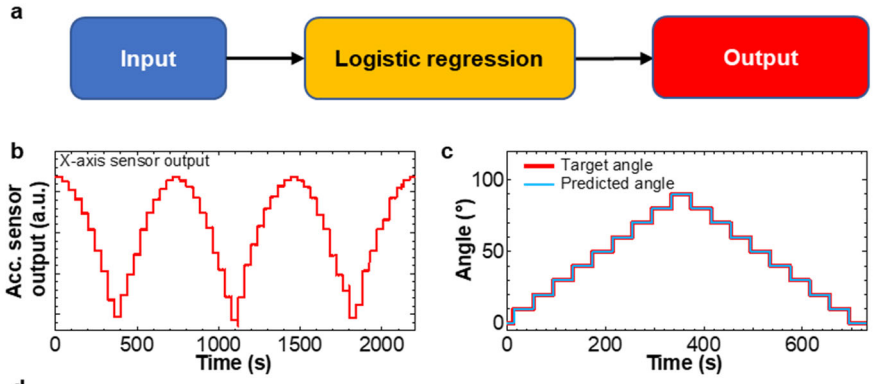

d

Cross validation (Accuracy)			
Trial1	Trial2	Trial3	Ave
0.997	0.998	0.997	0.997

Figure 4. Tilt angle prediction using logistic regression. (a) Schematic of the algorithm to predict tilt angle. (b) Acceleration sensor output as a function of tilt angle for the training dataset. (c) Predicted angle from X-axis results of the acceleration sensor. (d) Cross validation accuracy of each trial.

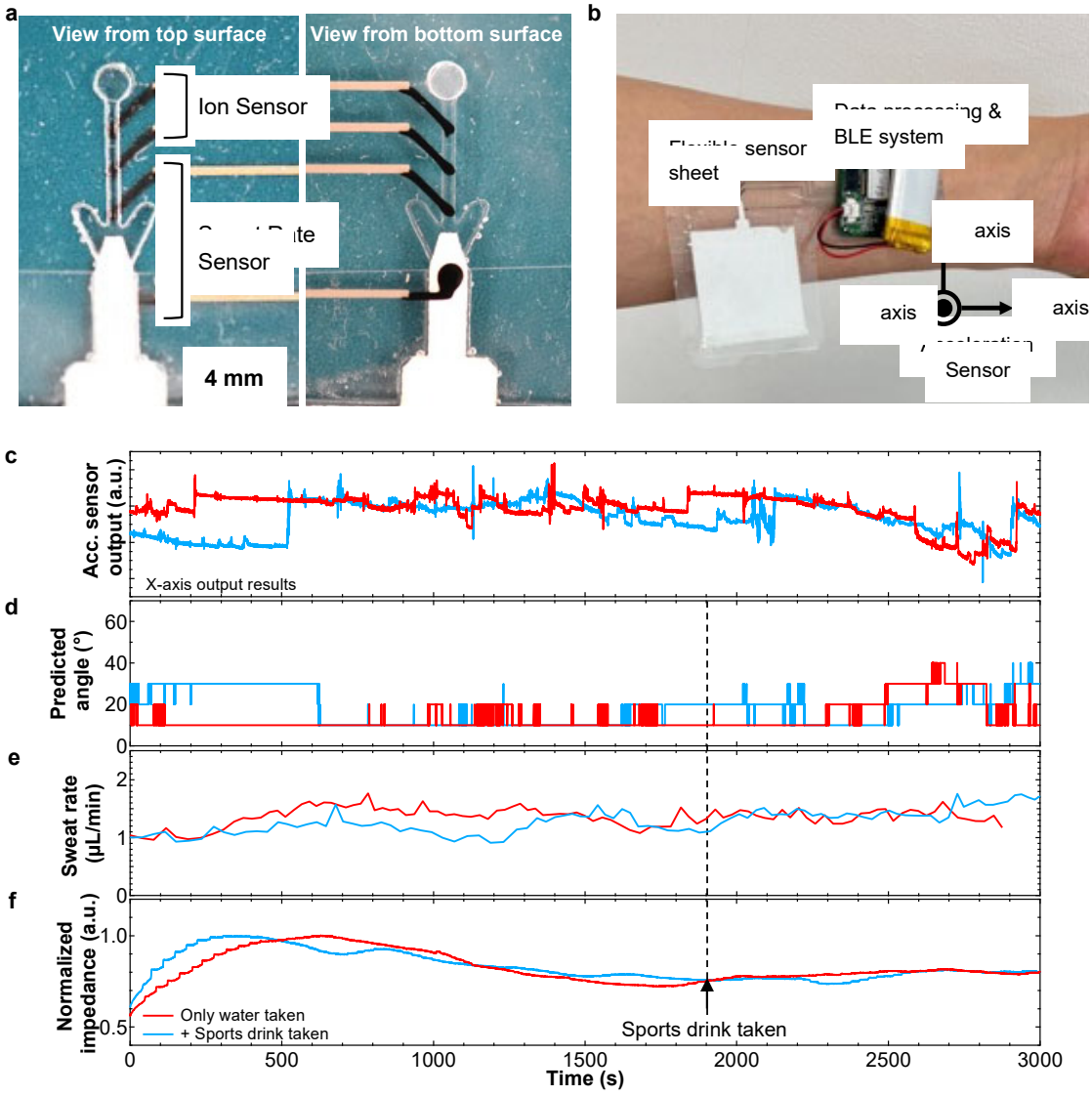

Figure 5. Wireless integrated sensor system and demonstration. Views of (a) the sweat sensor top surface and bottom surface and (b) sensor system worn on a subject's forearm. Real-time monitoring of (c) X- axis acceleration sensor output, (d) predicted angle, (e) sweat rate, and (f) normalized impedance during perspiration.

TOC

Continuous long-time sweat rate and electrolyte impedance sensors are integrated on flexible films. By optimizing the device structures, >11 times volume of sweat continuously is realized for electrical perspiration sensor compared to others reported previously. Furthermore, physiological responses by measuring perspiration rhythm changes extracted from real-time, continuous sweat impedance and rate are successfully monitored.

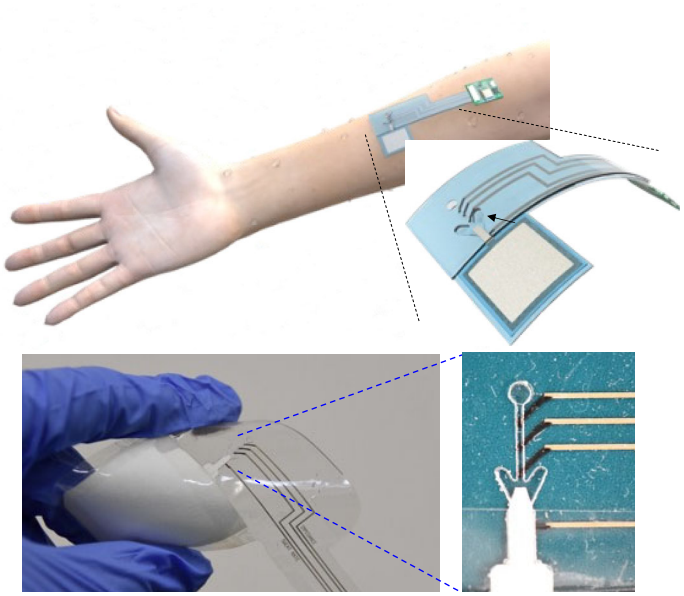

Supporting information

Wireless, flexible, ionic, perspiration-rate sensor system with long-time and high sweat volume functions toward early-stage, real-time detection of dehydration

*Satoko Honda[1†], Ryuki Tanaka[1†], Guren Matsumura[1], Naruhito Seimiya[1], Kuniharu Takei[1,2]**

[1]Department of Physics and Electronics, Osaka Metropolitan University, Naka-ku, Sakai, Osaka 599-8531, Japan

[2]Graduate School of Information Science and Technology, Hokkaido University, Kita-ku, Sapporo, Hokkaido 060-0814, Japan

†These authors contributed equally.

*Corresponding author: takei@ist.hokudai.ac.jp

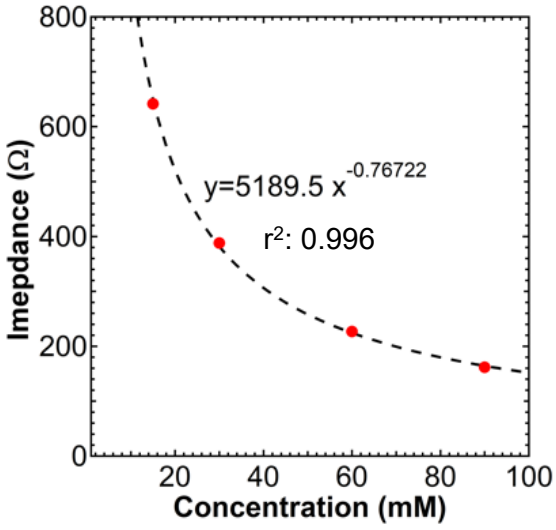

Figure S1. Impedance as a function of Na^+ concentration and an approximate curve.

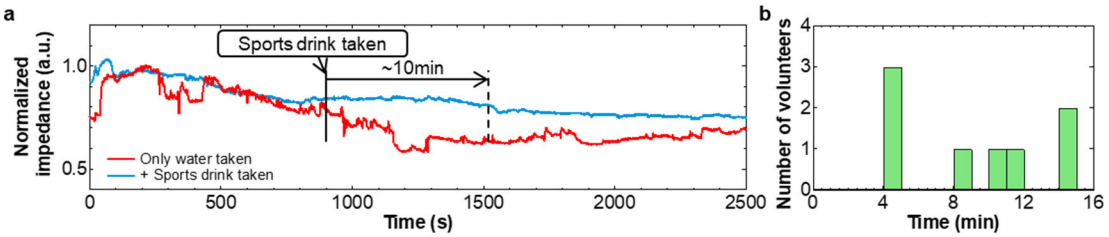

Figure S2. Effect of sports drink showing the time delay. (a) Real-time monitoring results with/without sports drink. (b) Numbers of volunteers and time lag after intake of sports drink.

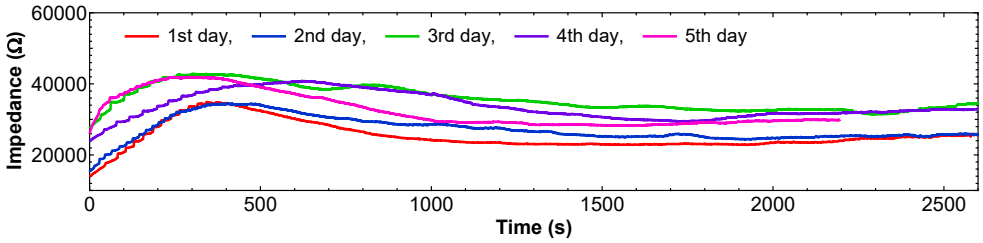

Figure S3. Multiple sweat impedance measurements for a week using the same sensor.

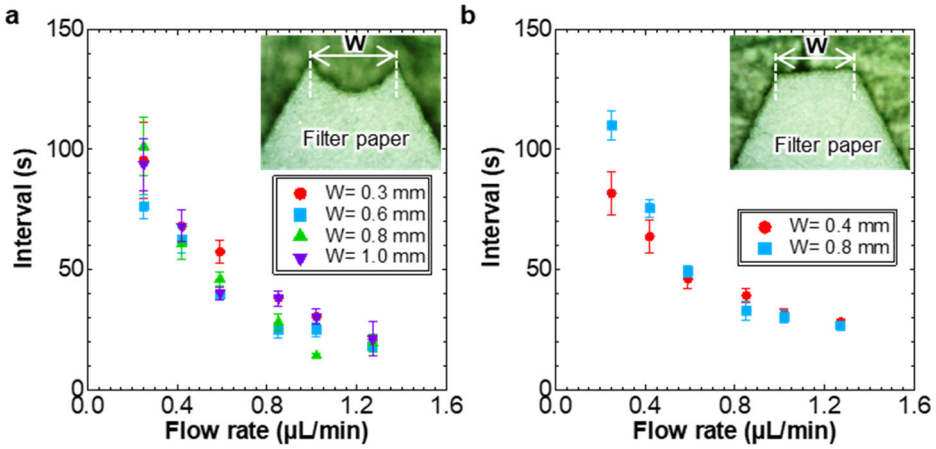

Figure S4. Sweat rate sensor with different shapes and widths of filter paper. (a) Interval as a function of flow rate in filter paper with curved tips and different widths. (b) Interval as a function of flow rate in filter paper with flat tips and different widths.

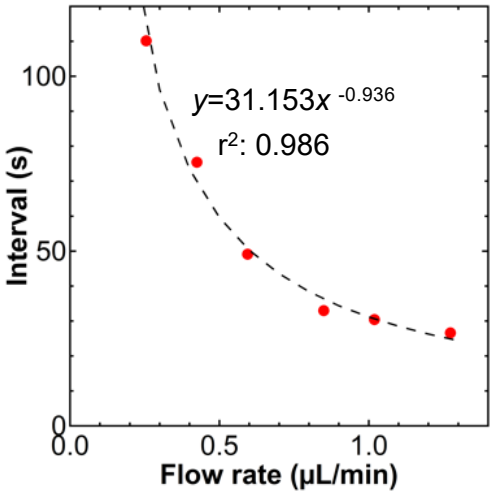

Figure S5. Interval as a function of flow rate and an approximate curve.

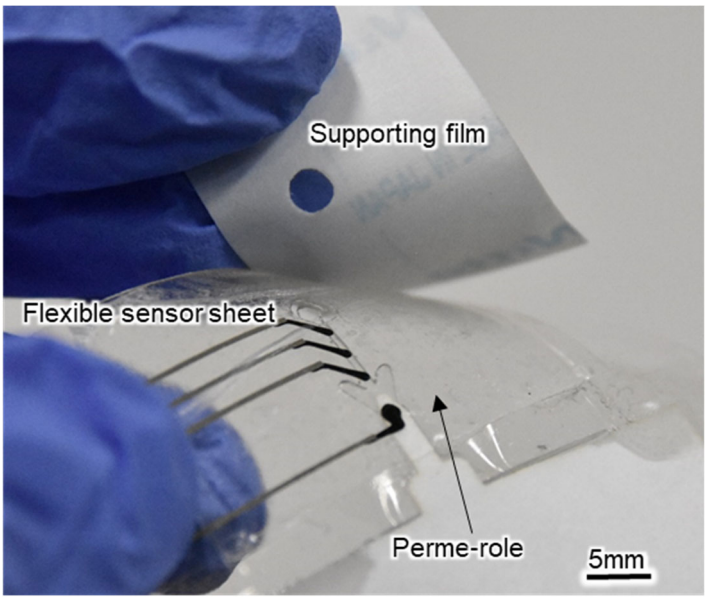

Figure S6. Photo of the flexible sensor sheet and supporting film.